


Design and Assessment of a 6-DOF Micro/Nanopositioning System

Defu Zhang , Pengzhi Li, Jianguo Zhang, Huanan Chen, Kang Guo, and Mingyang Ni

Abstract—A six degree-of-freedom (6-DOF) parallel positioning system with high resolution, high repeatability, and low parasitic motions was proposed. It mainly consists of three identical limbs. Each limb consists of two symmetrical six prismatic-universal-spherical branches. First, the design process for a novel 6-DOF limb with input displacement reduction was introduced. By applying bipods and linear displacement output mechanisms, these novel limbs with symmetric configurations were designed. Moreover, a numerical compliance/stiffness model of the proposed mechanism was built based on the matrix method. This numerical model was verified by ANSYS finite-element analysis (FEA) software package. Hence, the input stiffness, the output compliance, and the stroke of the mechanism can be theoretically estimated. Furthermore, a prototype made of stainless steel 431 was successfully manufactured by wire electrical discharge machining process. It is actuated and sensed by piezoactuators and capacitive displacement sensors, respectively. Finally, the working performances of this proposed mechanism were experimentally investigated. It shows that the spatial resolution can be achieved in $10 \text{ nm} \times 10 \text{ nm} \times 5 \text{ nm} \times 100 \text{ nrad} \times 100 \text{ nrad} \times 200 \text{ nrad}$ in an open-loop control. The closed-loop positioning accuracy in 3σ (σ , standard error) can reach $30 \text{ nm} \times 30 \text{ nm} \times 15 \text{ nm} \times 150 \text{ nrad} \times 150 \text{ nrad} \times 300 \text{ nrad}$. The experimental results not only validate the effectiveness of the proposed positioning system but also verify the nanometer-scale spatial positioning accuracy within several tens of micrometers stroke range. The proposed micro/nanopositioning system may expand the actual application of alignment optical elements in projection lenses of 193 nm immersion lithography.

Index Terms—Flexure mechanisms, mechanical design, micro/nanopositioning, parallel positioning system, six degree-of-freedom (6-DOF).

Manuscript received June 20, 2018; revised February 3, 2019 and June 5, 2019; accepted July 10, 2019. Date of publication August 7, 2019; date of current version October 15, 2019. Recommended by Technical Editor Y. K. Yong. This work was supported in part by the National Natural Science Foundation of China under Grant 61504142 and Grant 61604150, in part by the Science and Technology Development Project of Jilin Province under Grant 20170520102JH, and in part by the National Science and Technology Major Special Fund under Grant 2009ZX02205 and Grant 2016ZX02201. (Corresponding author: Defu Zhang.)

The authors are with the Changchun Institute of Optics, Fine Mechanics and Physics, Chinese Academy of Sciences, Changchun 130033, China (e-mail: zhangdf@sklao.ac.cn; kindrobot@163.com; zhangjg@ciomp.ac.cn; chennyhit@163.com; guok@sklao.ac.cn; mingyang.neal@gmail.com).

Color versions of one or more of the figures in this article are available online at <http://ieeexplore.ieee.org>.

Digital Object Identifier 10.1109/TMECH.2019.2931619

I. INTRODUCTION

MICRO/NANOPOSITIONING technology becomes much more essential in precision engineering, such as atomic force microscope system [1], microelectromechanical system [2], lithography [3], ultraprecision machining [4], and so on. In general, compliant mechanism can transmit some accurate relative motions in micro/nanometer scale through elastic deformation [5], [6]. This kind of mechanism has so many advantages, such as avoiding energy losses caused by friction, unnecessary of lubrication, absence of hysteresis, compactness, easy to be fabricated, position resolution in micro/nanometer scale, and so on. Hence, compliant mechanism becomes much more suitable for high-precision positioning applications than the conventional mechanism.

There are two types of compliant mechanisms named as serial and parallel mechanism, respectively. On one hand, the serial mechanism connects multiple lower mobility mechanisms in a nested or stacked manner [7]–[9]. Although the structure scheme and control strategy are simple in serial mechanism, it has low natural frequency, large inertia, error accumulation, and huge differences in dynamic characteristics of each motion element. The inconsistent performance of each motion axis in the workspace cannot be negligible. On the other hand, parallel mechanism connects an end effector by a series of individual limbs [10]–[12]. It is advantageous in high load capacity, small inertia, and especially negligible differences in dynamic characteristics of each motion axis with high motion accuracy [13]–[15]. Therefore, the parallel mechanism is more suitable and applicable for a micro/nanopositioning system. However, the end effector of parallel mechanism is directly connected with several limbs, resulting in the parasitic motions. Parasitic motion produces more than one direction of displacement, which is a typical character of parallel mechanism [16], [17]. Therefore, it is worth to pay much more attention to the compliant mechanism design to reduce the parasitic motion.

Over the past few decades, several piezoelectrically driven compliant parallel mechanisms have been reported [18]–[21]. Some successful commercial applications have emerged in market (e.g., the multiaxis positioners fabricated by Physik Instrumente GmbH and Company). Recently, more and more precision positioning systems with 6-DOFs, i.e., three linear and three rotational axes, are demanded in some special applications. The 6-DOF positioners make motion possible on the basis of complex trajectories in an arbitrary workspace. For example, Cai *et al.* [22] proposed a 6-DOF positioning system assembled by

two 3-DOF positioning platforms in series. The working space was $8.2 \mu\text{m} \times 10.5 \mu\text{m} \times 13.0 \mu\text{m} \times 224 \mu\text{rad} \times 105 \mu\text{rad} \times 97 \mu\text{rad}$ along the three linear and three rotational axes. Shin and Moon [23] reported a 6-DOF positioning system with double triangular parallel-positioning mechanisms. Three piezoelectric ceramic transducers (PZTs) were utilized in the inner triangle as in-plane positioning. The other three PZTs were mounted in the external triangle as out-of-plane positioning. The stroke of this mechanism exceeded $50 \mu\text{m} \times 50 \mu\text{m} \times 150 \mu\text{m} \times 733 \mu\text{rad} \times 733 \mu\text{rad} \times 244 \mu\text{rad}$. The translational and rotational resolutions were $0.1 \mu\text{m}$ and $1 \mu\text{rad}$, respectively. Moreover, a 6-DOF prismatic-spherical-spherical parallel compliant nanopositioner was introduced by Wu *et al.* [24]. This nanopositioner has a stroke of $7.49 \mu\text{m} \times 8.22 \mu\text{m} \times 8.79 \mu\text{m} \times 205 \mu\text{rad} \times 245 \mu\text{rad} \times 202 \mu\text{rad}$ with a translational resolution of 5 nm and a rotational resolution of $0.7 \mu\text{rad}$, respectively. Kang and Gweon [25] proposed a large-stroke 6-DOF micropositioning mechanism applied for optical alignment. The workspace was $\pm 2 \text{ mm} \times \pm 2 \text{ mm} \times \pm 2 \text{ mm} \times \pm 35 \text{ mrad} \times \pm 35 \text{ mrad} \times \pm 35 \text{ mrad}$ with a high translation resolution of 15 nm and a rotational resolution of $0.68 \mu\text{rad}$. Furthermore, based on the kinematic coupling principle, a 6-DOF micropositioning mechanism was designed in by Varadarajan and Culpepper [26], [27]. Although the designed stage can demonstrate a position resolution of 4 nm within a single-axis stroke, the resultant parasitic motion cannot be ignored. The z -axis parasitic motion exceeded $1 \mu\text{m}$ while driving the x -axis stroke of $\pm 25 \mu\text{m}$ or rotating the θ_x -axis with $200 \mu\text{rad}$. A 6-DOF parallel micro-manipulator with an alternative type of Stewart mechanism was also introduced by Yue *et al.* [28]. Its maximum translation and rotation errors reached 12.8% and 9.6% of the target motion, respectively. Hence, it is worth to develop a 6-DOF precision positioning system with high motion accuracy and low parasitic motion.

The main contribution of this article is that a novel 6-DOF micro/nanopositioning system that is featured with high resolution, high repeatability, and low parasitic motion has been proposed. This article includes the following sections. At first, mechanical design and assembly are outlined in Section II. As following, an analytical model that can be used to predict the stroke range and stiffness of the designed mechanism is established in detail in Sections III. Furthermore, the numerical design of the positioning system is verified by applying ANSYS finite-element analysis (FEA) in Section IV. Moreover, the static performances of the proposed mechanism are tested with a self-fabricated prototype in Section V. A series of experimental investigations are carried out in Section VI, in order to clarify the positioning accuracy and repeatability of the proposed mechanism. Finally, Section VII concludes this research article.

II. MECHANISM DESIGN

A. Configuration Design

To begin with, the DOFs of a limb in a flexure parallel mechanism are introduced. Gao *et al.* [29] pointed out that if a parallel mechanism has a certain DOFs ($\$$), the limbs

(1, 2, ..., n) connecting the end effector and the base need to satisfy the following equation:

$$\$ = \$_1 \cap \$_2 \dots \cap \$_n \quad (1)$$

where $\$_n$ is the DOFs of the n th limb. As known, Plücker coordinates are adopted as an effective way to assign six homogeneous coordinates to each line in the projective three-dimensional (3-D) space. $\$$ can be considered as the special Plücker coordinates in characterizing the output displacement of a limb. Equation (1) indicates that the special Plücker coordinates of the stage motion equal to the intersection of the special Plücker coordinates of all the limbs in the parallel mechanism.

Gao *et al.* [29] reported that a 6-DOF parallel mechanism can be actualized by three or six limbs, where each limb should have 6-DOFs. Parallel mechanisms with six limbs have commonly been used so far, such as the Stewart platform. These configurations usually include 6-SPS, 6-RSS, 6-PUS or 6-RUS, where P, R, U, and S are denoted as the prismatic, revolute, universal, and spherical joints, respectively. With considering that fewer limbs can achieve low cost, easy installation, high integration, and light weight, a novel 6/3-PUS flexure parallel mechanism with 6-DOFs is proposed in this article.

Hence, flexure hinges used in each limb are designed at first. In a flexure mechanism, hinges usually include revolute joints (R), prismatic joints (P), and universal joints (U), as shown in Fig. 1. The rotation hinge has only 1-DOF of y -axis rotation (R_y), as shown in Fig. 1(a). Hinges with parallel rotation joints have three DOFs, which are x -axis translation (T_x), R_y , and z -axis rotation (R_z), as shown in Fig. 1(b). Two rotating hinges are orthogonal to each other can be considered as a universal joint. It has three DOFs of x -axis rotation (R_x), R_y , and R_z , as shown in Fig. 1(c). Two universal joints that are connected in series have five DOFs, i.e., T_x , y -axis translation (T_y), R_x , R_y , and R_z , as shown in Fig. 1(d).

The limbs in Fig. 1(b), (c), and (d) can be obtained by series connection of multiple joints shown in Fig. 1(a), respectively. The limb, as shown in Fig. 1(e) and (f), can be obtained by connecting two identical hinges in parallel as introduced in Fig. 1(d). Although the single branch along the z -direction in Fig. 1(e) has 5-DOFs, i.e., T_x , T_y , R_x , R_y , and R_z , it is constrained by the horizontal branch along the x -direction. Hence, due to the constrained T_x , the limb has only 4-DOFs of T_y , R_x , R_y , and R_z . Similarly, horizontal branch along the x -direction also has 4-DOFs of T_y , R_x , R_y , and R_z . These two combined hinges constraint 2-DOFs of T_x and z -axis translation (T_z). This structure is well known as bipod [30]. Moreover, the stability of the mechanism shown in Fig. 1(f) is better than that shown in Fig. 1(e) when considering the load capacity of the end effector. However, the mechanisms shown in Fig. 1(e) and (f) require at least three times threading from three different directions with the wire electrical discharge machining (WEDM) process. The manufacture process becomes complex and time consuming. Although it just needs twice threading from two vertical directions with optimizing the structure as Fig. 1(g) shows, the rotational axis drift is increased due to the diamond shape of rotation hinge. Therefore, the structure was optimized, as shown in Fig. 1(h), to obtain not only the simple

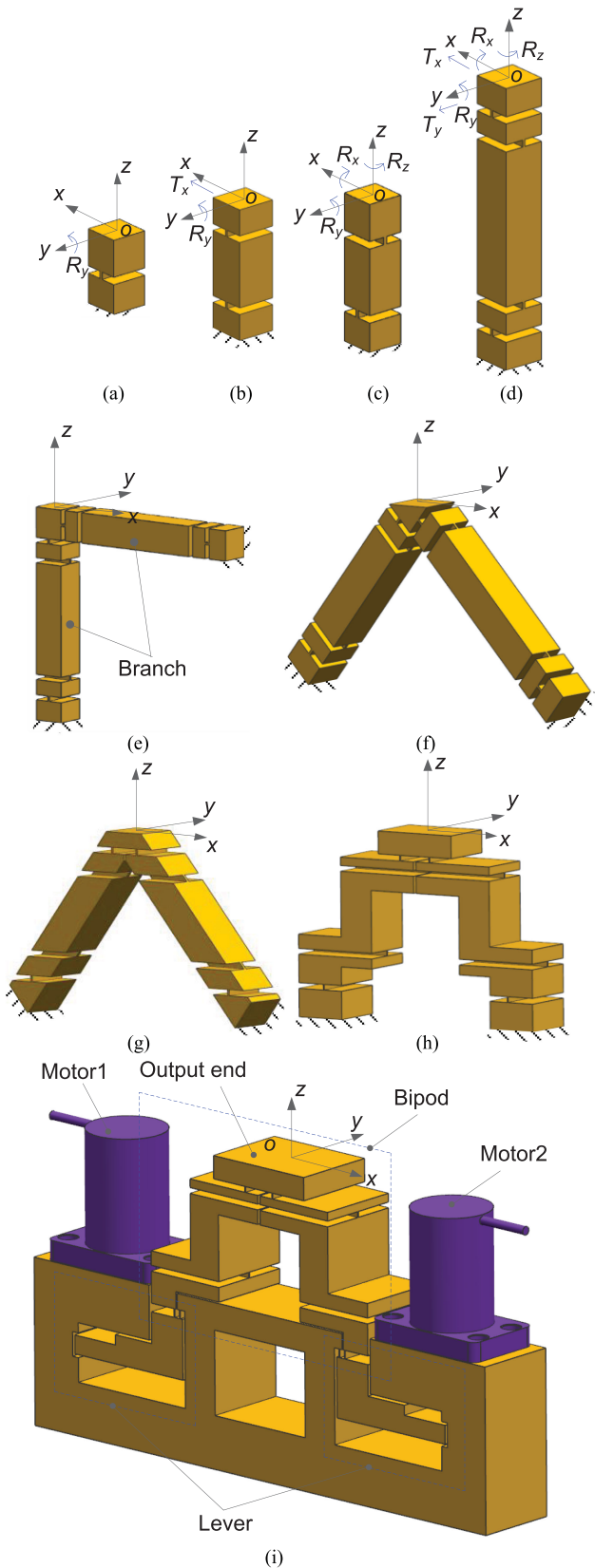


Fig. 1. Novel 6-DOF limb. (a) Revolute joint (R). (b) Prismatic joint (P). (c) Universal joint (U). (d) Two universal joints. (e) Bipod rotate 45° about y-axis. (f) Standard bipod. (g) Bipod easy fabricating type I. (h) Bipod easy fabricating type II. (i) Output-displacement-reduced 6-DOF limb.

manufacturing process but also the tiny rotational axis drift. Furthermore, if the driving motor is mounted at the bottom of each branch, as shown in Fig. 1(h), the output displacement of T_x and T_z can also achieve. The DOFs of T_x and T_z of the limb are not being constrained any more. Hence, a 6-DOF limb that satisfies (1) can be obtained.

B. Mechanism Assembly

In order to decrease the resolution requirement for a motor, a displacement reduction lever was also adopted to achieve tens of nanometers output resolution. As shown in Fig. 1(i), a 6-DOF limb with a bipod and two levers (LBL) is proposed. The output ends of levers are connected with the two fixed ends of the branch, as shown in Fig. 1(h). A reduced T_z displacement of the output end is generated when two linear actuators move in the same direction. A reduced T_x displacement is obtained when two linear actuators move in the opposite direction. When only one actuator moves, a reduced translation in the xz -plane is obtained.

In order to reduce the input parasitic motion, a hook joint is mounted between the motor and the lever. It transmits only the axial force and protects the motor from undesired shear forces and bending moments. It should be noted that an LBL limb can also be changed into other forms. For example, both the output direction and displacement can be changed by substituting a Scott Russell mechanism or a four-bar mechanism for levers.

The designed 6-DOF parallel positioning system is shown in Fig. 2(a), where three identical 6-DOF limbs are uniformly distributed around the z -axis with 120° intervals. By controlling the input displacement of the six linear actuators, these three limbs can do the synchronous motion. Hence, the end effector can achieve the posture adjustments with 6-DOF in the 3-D space. The maximum diameter and height of the 6-DOF mechanism are 264 mm and 148.4 mm, respectively. The computer-aided design (CAD) model and the assembly process of the proposed mechanism are illustrated in Fig. 2(b).

III. MECHANISM MODELING

There are several methods that can be used for modeling the elastic deformation of flexure mechanisms. The commonly used methods are pseudo-rigid-body (PRB) model [31] and Castigliano's second theorem [32]. The PRB model is suitable for planar structure while Castigliano's second theorem requires complex mechanical analysis in a linearly elastic structure. As compared with the above-mentioned methods, the compliance matrix method (CMM) which is derived from the linear Hooke's law [11], [19], [33] is much more efficient in modeling the complex space flexure mechanism. Hence, the CMM method was adopted to establish the stiffness/compliance model of the proposed mechanism in this article.

A. Compliance of the LBL Limb

The system consists of three LBL limbs connected in parallel. First, the output compliance of Limb1 in the B - xy coordinate

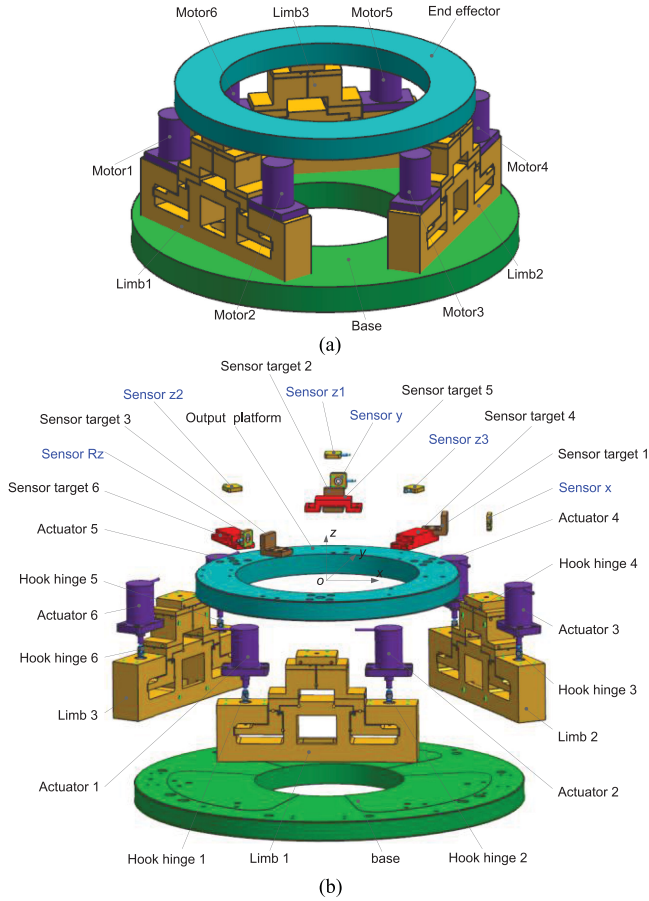


Fig. 2. Positioning system of 6-DOF is designed in this article. (a) Composition of the positioning system. (b) CAD model of the positioning system, the connecting screws, and sensor clamps are removed for clear observation.

system, as shown in Fig. 3, is investigated. The geometrical dimension of Limb1 is also shown in Fig. 3. Hook hinge O_2O_3 and hinge O_4O_5 are connected in parallel in the O_6 - xy coordinate system. The compliance of position O_6 with respect to O_1 and O_4 is given by

$$\mathbf{C}_6 = \left(\left(\mathbf{T}_3^6 \cdot \mathbf{C}_{\text{hook}} \cdot (\mathbf{T}_3^6)^T \right)^{-1} + \left(\mathbf{T}_5^6 \cdot \mathbf{C}_5 \cdot (\mathbf{T}_5^6)^T \right)^{-1} \right)^{-1} \quad (2)$$

where \mathbf{C}_{hook} and \mathbf{C}_5 are the local compliances of the hook hinge O_2O_3 and hinge O_4O_5 , and \mathbf{T}_3^6 and \mathbf{T}_5^6 are the transformation matrices from coordinate systems O_3 - xy and O_5 - xy to O_6 - xy .

Similarly, the hinges O_6O_7 , O_8O_9 , $O_{10}O_{11}$, and $O_{12}O_{13}$ are connected in series to the B - xy coordinate system and the compliance can be calculated by

$$\mathbf{C}_B^6 = \sum_{i=3}^6 \mathbf{T}_{2i+1}^B \cdot \mathbf{C}_{2i+1} \cdot (\mathbf{T}_{2i+1}^B)^T \quad (3)$$

where \mathbf{C}_{2i+1} (for $i = 3, 4, 5$, and 6) are the local compliance and \mathbf{T}_{2i+1}^B are the transformation matrices.

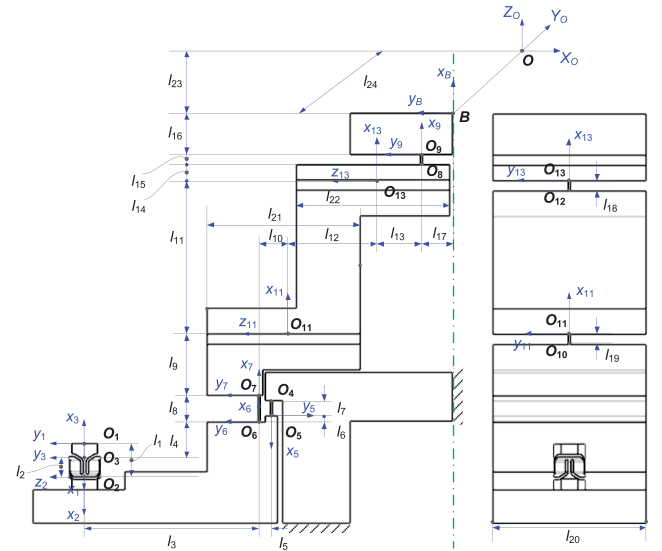


Fig. 3. Geometric dimension of the left part in Limb1.

The compliance of the left branch in the B - xy coordinate system is

$${}_l\mathbf{C}_B = \mathbf{C}_B^6 + \mathbf{T}_6^B \cdot \mathbf{C}_6 \cdot (\mathbf{T}_6^B)^T \quad (4)$$

where \mathbf{T}_6^B is the transformation matrix.

And then, since the Limb1 is left-right symmetric about the x -axis, two of the same branches, as shown in Fig. 3, are connected in parallel at point B . Hence, the resultant compliance of the Limb1 in the B - xy coordinate system can be derived as

$$\mathbf{C}_B = \mathbf{K}_B^{-1} = \left(({}_l\mathbf{C}_B)^{-1} + (\mathbf{T}_r^l \cdot ({}_l\mathbf{C}_B) \cdot (\mathbf{T}_r^l)^T)^{-1} \right)^{-1} \quad (5)$$

where the transformation matrix from the right to left branch can be expressed by

$$\mathbf{T}_r^l = \begin{bmatrix} \mathbf{R}_x^\pi & \mathbf{0} \\ \mathbf{0} & \mathbf{R}_x^\pi \end{bmatrix} \quad (6)$$

where \mathbf{R}_x^π represents rotation matrix that rotates π angle about the x -axis.

B. Output Compliance of the End Effector

According to the system design in Fig. 2, the output compliance model of each limb is same at each respective output ends. Those three limbs are connected in parallel at the centroid point O of the output end. The output compliance of the limbs at the centroid point O can be obtained as

$$\mathbf{C}_O = \left(\sum_{i=1}^3 \mathbf{K}_i^O \right)^{-1} = \left(\sum_{i=1}^3 (\mathbf{T}_i^O \cdot \mathbf{C}_i \cdot (\mathbf{T}_i^O)^T)^{-1} \right)^{-1} \quad (7)$$

where \mathbf{C}_i (for $i = 1, 2$, and 3) is the local compliance of each limb at its own output end and the transformation matrix \mathbf{T}_i^O

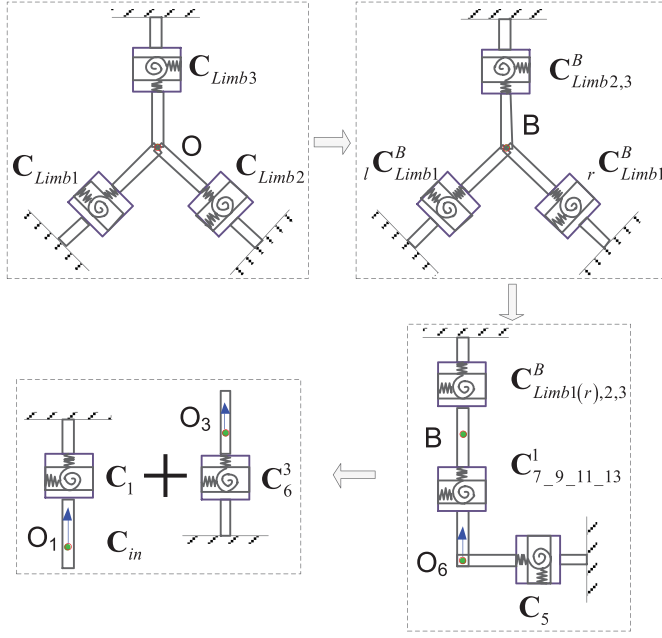


Fig. 4. Stiffness model of the mechanism with only one limb actuated.

can be written as

$$\mathbf{T}_i^O = \begin{bmatrix} \mathbf{R}_i^O & \mathbf{R}_i^O \cdot \mathbf{S}(\mathbf{r}_i^O) \\ \mathbf{0} & \mathbf{R}_i^O \end{bmatrix}$$

where \mathbf{R}_i^O is the rotation matrix of the coordinate B_i with respect to O , \mathbf{r}_i^O is the position vector of the point B_i expressed in reference frame O , and $\mathbf{S}(\mathbf{r})$ represents the skew-symmetric operator for a vector $\mathbf{r} = [r_x \ r_y \ r_z]^T$ with the notation

$$\mathbf{S}(\mathbf{r}) = \begin{bmatrix} 0 & -r_z & r_y \\ r_z & 0 & -r_x \\ -r_y & r_x & 0 \end{bmatrix}.$$

C. Input Stiffness of the Mechanism

To calculate the input stiffness, the stiffness model of the proposed system can be illustrated in Fig. 4. Limb2 and Limb3 are connected in parallel at the center O of the platform. And then, the compliance at the reference point B of Limb1 can be derived as

$$\mathbf{C}_{Limb2,3}^B = (\mathbf{T}_O^B)^T \left((\mathbf{C}_{Limb2}^O)^{-1} + (\mathbf{C}_{Limb3}^O)^{-1} \right)^{-1} (\mathbf{T}_O^B)^T \quad (8)$$

where \mathbf{C}_{Limb2}^O and \mathbf{C}_{Limb3}^O are the compliances of Limb2 and Limb3 at O and \mathbf{T}_O^B is the transformation matrix.

Limb2 and Limb3 are connected in parallel at B , the compliance is $\mathbf{C}_{Limb2,3}^B$. Then, $\mathbf{C}_{Limb2,3}^B$ and Limb1's right branch $r\mathbf{C}_{Limb1}^B$ are parallel in the coordinate system B -xy. So, the parallel compliance at B can be calculated as

$$\mathbf{C}_{Limb1(r),2,3}^B = \left((r\mathbf{C}_{Limb1}^B)^{-1} + (\mathbf{C}_{Limb2,3}^B)^{-1} \right)^{-1}. \quad (9)$$

TABLE I
STRUCTURE PARAMETERS OF THE MECHANISM

l_1	l_2	l_3	l_4	l_5	l_6	l_7	l_8
5.0	2.0	34.3	13.2	2.4	1.2	3.0	5.2
l_9	l_{10}	l_{11}	l_{12}	l_{13}	l_{14}	l_{15}	l_{16}
12.0	4.8	29.7	17.5	9.5	3.3	2.0	8.0
l_{17}	l_{18}	l_{19}	l_{20}	l_{21}	l_{22}	l_{23}	l_{24}
6.0	2.0	2.0	30.0	30.0	30.0	20.0	112.0

Units: mm.

TABLE II
MATERIAL PARAMETERS OF THE MECHANISM

Materials	Young's Modulus /GPa	Density kg/m ³	Poisson's Ratio	Yield strength /MPa
431	198.6	7.75×10^3	0.27	655~1080
60Si2Mn	206	7.85×10^3	0.27	1175

The parallel compliance of position B is transformed into the coordinate system O_6 -xy and connected in series with the hinges O_6O_7 , O_8O_9 , $O_{10}O_{11}$, and $O_{12}O_{13}$. The compliance of position O_6 with respect to the fixed end can be obtained as

$$\mathbf{C}_B^6 = \mathbf{T}_B^6 \cdot \mathbf{C}_{Limb1(r),2,3}^B \cdot (\mathbf{T}_B^6)^T + \sum_{i=3}^6 \mathbf{T}_{2i+1}^6 \cdot \mathbf{C}_{2i+1} \cdot (\mathbf{T}_{2i+1}^6)^T \quad (10)$$

where \mathbf{T}_B^6 is the transformation matrix.

The compliance of position O_6 is connected in parallel with the hinge O_4O_5 in the coordinate system O_3 -xy

$$\mathbf{C}_6^3 = \left(\left(\mathbf{T}_6^3 \cdot \mathbf{C}_B^6 \cdot (\mathbf{T}_6^3)^T \right)^{-1} + \left(\mathbf{T}_5^3 \cdot \mathbf{C}_5 \cdot (\mathbf{T}_5^3)^T \right)^{-1} \right)^{-1} \quad (11)$$

where \mathbf{T}_6^3 and \mathbf{T}_5^3 are the transformation matrices.

Then, the above compliance and hook hinge O_2O_3 are connected in series at the input O_1

$$\mathbf{C}_{in} = \mathbf{T}_3^1 \cdot \mathbf{C}_6^3 \cdot (\mathbf{T}_3^1)^T + \mathbf{C}_{hook} \quad (12)$$

where \mathbf{T}_3^1 is the transformation matrix.

Finally, we can get the input stiffness

$$k_{in} = [\mathbf{C}_{in} (1, 1)]^{-1}. \quad (13)$$

IV. MODEL VALIDATION WITH FEA

To verify the feasibility of the above proposed numerical model, the output compliance, input stiffness, and motion stroke of the proposed mechanism, the FEA process by ANSYS workbench software package is carried out in this section. The material was stainless steel 431. The mechanical dimension of the proposed mechanism in Fig. 3 is detailedly given in Table I. Its physical and mechanical properties are concluded in Table II. In the FEA process, a 3-D FEA model is established with the SOLID186 and SOLID5. A smaller mesh size is defined at the hinge cut-out position to obtain an accurate simulation result. The bases of those three limbs are fixed in the FEA.

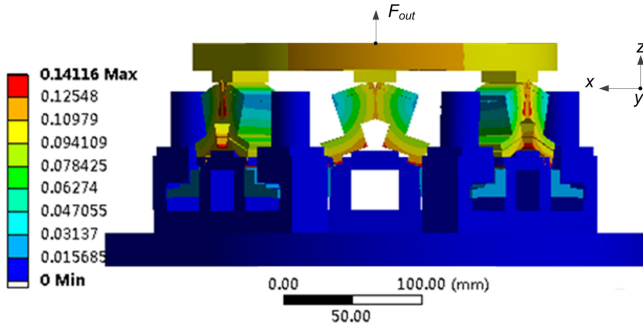


Fig. 5. Mechanism deformation along the z -axis with a force of 1800 N on the end effector (enlarged 110 times for a clear view).

A. Output Compliance and Input Stiffness

First, the stiffness/compliance and stroke of the proposed mechanism were analyzed by the static FEA. In order to calculate the input stiffness, a certain force F_{in} was applied to the input end of Limb1. And then, the corresponding input displacement was extracted from the FEA to obtain the input stiffness. In addition, by applying a certain force F_{out} to the end effector, the output compliance can be evaluated by extracting the platform displacement, as shown in Fig. 5.

Based on (7) and (13), the output compliance and the input stiffness are predicted to be 8.479×10^{-8} m/N and 1.229×10^4 N/m, respectively, by the CMM models. By the FEA simulation results, the output compliance and the input stiffness are 7.436×10^{-8} m/N and 1.041×10^4 N/m, respectively. The model deviations are 14.02% and 18.06% according to an error equation $(\text{CMM-FEA})/\text{FEA} \times 100\%$. These deviations are mainly caused by some assumptions in the numerical analytical model, such as the accuracy of the compliance equations, the neglect of the links compliance between hinges, and so on. Moreover, the linear relationship between the input force and input displacement indicates that stress stiffening does not happen in the proposed mechanism.

B. Stroke

When a motor supplies a linear displacement of 0.5 mm to the input end of each limb, the maximum stress of 181.87 MPa subject to the axial load is generated at position O_7 of limbs of the proposed mechanism. Therefore, the safety factor can be calculated as $\sigma_y/\sigma_{\max} = 655 \text{ MPa}/181.87 \text{ MPa} = 3.6$, where σ_{\max} is the maximum allowable stress of the material. It indicates that the proposed mechanism can achieve reliably long-term running with the elastic deformation. The high-precision positioning repeatability can also be guaranteed. With a maximum input displacement not more than 0.5 mm at input ends of three limbs, the 6-DOF strokes of the end effector are also investigated by the FEA. The T_x , T_y , and T_z strokes are $59.441 \mu\text{m}$, $67.33 \mu\text{m}$, and $37.786 \mu\text{m}$, respectively. The R_x , R_y , and R_z strokes are $326.477 \mu\text{rad}$, $350.25 \mu\text{rad}$, and $512.801 \mu\text{rad}$, respectively.

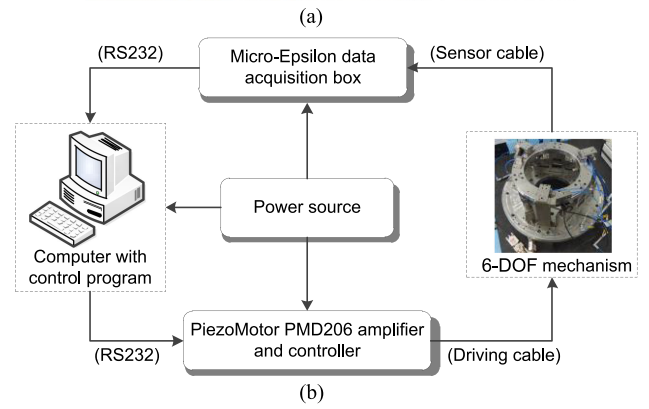
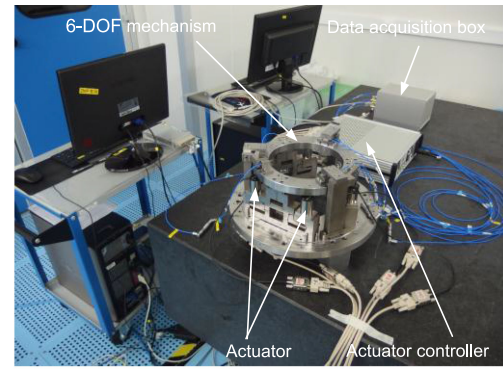


Fig. 6. Experimental setup. (a) Photograph of the positioning system. (b) Hardware connection.

C. Modal Analysis

The constraint modal analysis was performed. It demonstrates that the 1st and 2nd natural frequencies are 188.84 Hz and 189.02 Hz, respectively. They are translational vibrations in the xy -plane. The third mode is the rotation around the z -axis, which is 231.89 Hz. The bending vibrations around R_x/R_y -axis and the translation vibrations along the z -axis happen in the 4th, 5th, and 6th modes, respectively. The 4th and 5th modes are close to each other with the vibration frequency of 331.53 Hz and 331.66 Hz, respectively. The 6th mode is a translation along the z -axis with a frequency of 364.22 Hz.

V. PROTOTYPE FABRICATION AND TESTS

In this section, the working performances of the proposed positioning system were experimentally investigated with a fabricated prototype.

A. Experimental Setup

The fabricated prototype and the experimental configurations are shown in Fig. 6. Capacitive displacement sensors are used to measure the postures of the end effector. The base of this system was fixed to a vibration isolation platform preventing the vibration from ground. Each limb was fabricated by the WEDM process, and the material is stainless steel 431. The end effector was bolted to three limbs and then mounted on the

base holistically. Each limb was actuated by two piezoactuators (LTC40 from PiezoMotor) with a stroke of ± 1.5 mm and a submicro/nanometer positioning resolution. The driving voltage of 0–48 V can be obtained from a six-axis piezoamplifier and controller (Driver 206 from PiezoMotor). The piezoelectric actuator was connected with a hook hinge. There was no gap between the motor and the mechanism during operation. Hence, it becomes unnecessary to carry out the preloading springs. In order to measure the six motion DOFs of the proposed mechanism, six measuring blocks were mounted on the end effector. The output motion of the end effector was measured by six capacitive displacement sensors (CSH05FL from MicroEpsilon) which have a linearity of $\pm 0.05\%$ in a full stroke of 500 μm . The static and dynamic resolutions are 0.38 nm and 10 nm under the sampling rate of 2 Hz and 8.8 kHz. The analog output voltage of the six sensors was changed into digital output by a data acquisition box. Then, the digital output was picked up by a computer through a RS232 interface with a sampling frequency of 10 Hz. It should be noted that the measure direction of each sensor is the same as the motion direction of the measured target, which is beneficial for eliminating Abbe errors.

B. Open-Loop Performance Testing

In this section, the position resolution of the proposed mechanism was experimentally investigated by the open-loop control. The T_x response was studied by using a continuous-step command with a position resolution of 0.01 μm , as shown in Fig. 7(a). Because the response speed is slow, the position overshoot of this positioning system is negligible. It also shows that the steady-state error remains within the range of ± 5 nm, which verifies that the position resolution of T_x is about 10 nm. Similarly, the position resolution of T_y is also about 10 nm in the proposed mechanism, as shown in Fig. 7(b). In addition, the position resolution of T_z was also investigated. In Fig. 7(c), it shows that the position step of 5 nm can be clearly identified, and the tracking steady-state error is also within ± 2.5 nm. It indicates that the position resolution of T_z can achieve about 5 nm. Furthermore, the angular resolutions of $R_x/R_y/R_z$ are measured as 100 nrad, 100 nrad, and 200 nrad, respectively, as shown in Fig. 7(d)–(f).

Moreover, with a maximum actuators' input displacement of 0.5 mm, the stroke of the proposed mechanism was also investigated with an open-loop control. The stroke is about $\pm 40 \mu\text{m} \times \pm 40 \mu\text{m} \times \pm 30 \mu\text{m} \times \pm 200 \mu\text{rad} \times \pm 200 \mu\text{rad} \times \pm 300 \mu\text{rad}$ in the 3-D space. Due to the manufacturing errors and motor assembly tolerances, the actual two-direction travel range is not exactly symmetrical about the zero point.

And then, the parasitic motion of the end effector was investigated. Experiments were carried out with an open-loop control. When controlling the end effector just move along the x -axis direction within $\pm 40 \mu\text{m}$, the displacement of T_x and the other five parasitic motions (T_y , T_z , R_x , R_y , and R_z) are simultaneously measured. Fig. 8(a) illustrated the experimental results. The maximum translational parasitic errors of T_y and T_z are 0.426 μm and $-0.139 \mu\text{m}$, respectively. The ratio of the parasitic error to the primary motion in T_y and T_z is about 1.064% and 0.348%, respectively. Similarly, the maximum

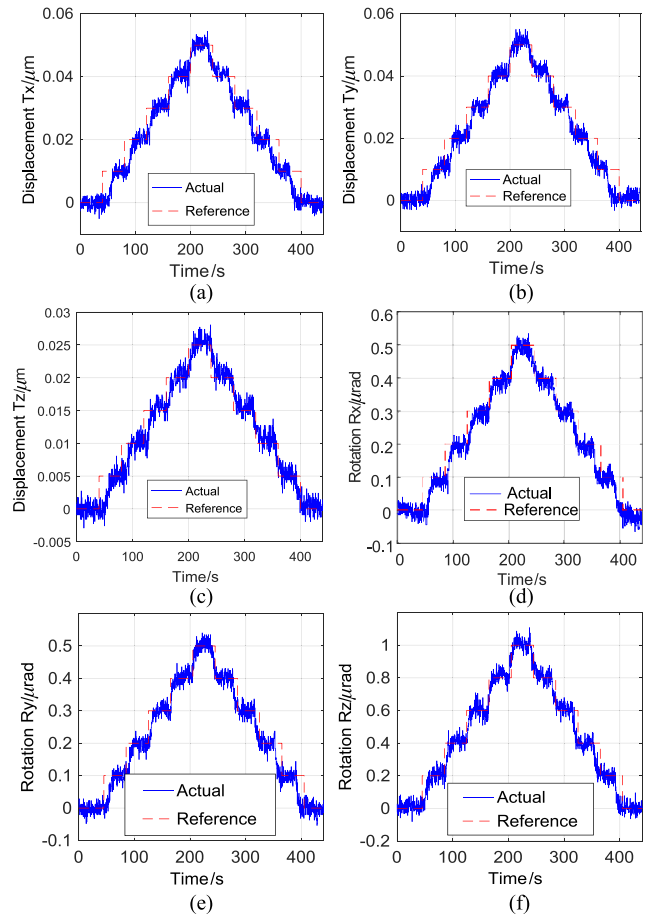


Fig. 7. Open-loop resolution results of the consecutive steps. (a) Response of T_x resolution. (b) Response of T_y resolution. (c) Response of T_z resolution. (d) Response of R_x resolution. (e) Response of R_y resolution. (f) Response of R_z resolution.

parasitic errors for $R_x/R_y/R_z$ are measured as $-0.915 \mu\text{rad}$, $-2.521 \mu\text{rad}$, and $-7.748 \mu\text{rad}$, respectively. So, the ratio of the parasitic error to the primary motion in R_x , R_y , and R_z is 2.288%, 6.48%, and 19.369%, respectively. With the same investigation methods, the parasitic errors can also be obtained when just driving the end effector along the T_y , T_z , R_x , R_y , and R_z direction, as shown in Fig. 8(b)–(f).

It is considered that there are several reasons causing the parasitic motion generation in an open-loop control, such as manufacturing error, misalignment of motors, assembly errors, mounting error of sensors, Abbe errors between the motion axes and the measurement point, and so on. The above mentioned conditions also decrease the positioning accuracy of the proposed mechanism in an open-loop control. Parasitic errors may be reduced by adjusting the sensor installation with a coordinate measuring machine. In order to increase the positioning accuracy and decrease the parasitic motion, a closed-loop control was applied to the proposed positioning system.

VI. EXPERIMENTAL TESTS AND DISCUSSIONS

In this section, the positioning performance of the proposed system was experimentally investigated with a closed-loop control.

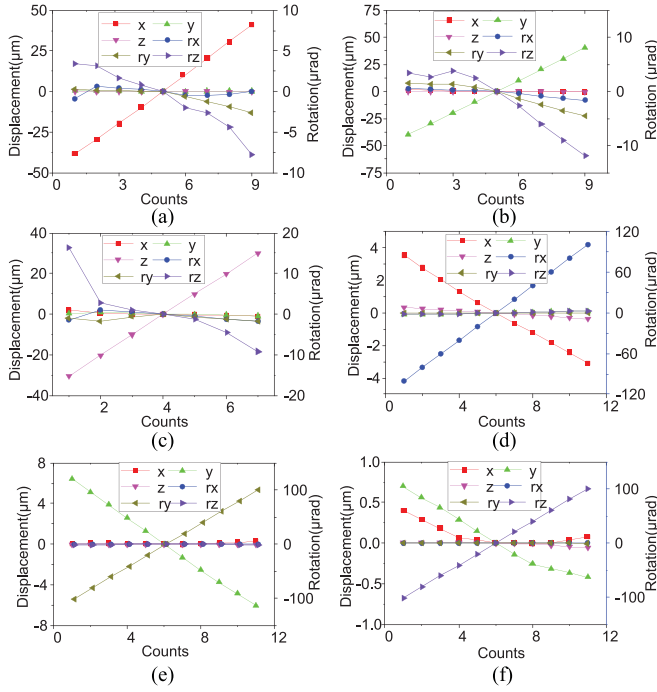


Fig. 8. Parasitic errors of the end effector. (a) T_x primary motion. (b) T_y primary motion. (c) T_z primary motion. (d) R_x primary motion. (e) R_y primary motion. (f) R_z primary motion.

A. Positioning Accuracy in Six-Axis Control

The positioning accuracy was investigated by moving the end effector from an initial position (0, 0, 0, 0, 0, 0) to a target position (10 μm , 10 μm , 10 μm , 100 μrad , 100 μrad , 100 μrad) with controlling all the six motion axis simultaneously. The measurement results are shown in Fig. 9. It shows that the finally achieved position is (10.000 μm , 10.005 μm , 9.998 μm , 99.973 μrad , 99.961 μrad , and 99.937 μrad). The positioning processes are shown in Fig. 9(a)–(f). The steady-state errors at the target position are enlarged view in Fig. 9(g)–(l), and the corresponding histograms of those steady-state errors are shown in Fig. 9(m)–(r). The 3σ positioning accuracy of $T_x/T_y/T_z/R_x/R_y/R_z$ is 21.69 nm, 18.92 nm, 10.71 nm, 86.43 nrad, 87.78 nrad, and 200.51 nrad, respectively.

With controlling the entire six motion axis simultaneously in a close-loop control, the positioning repeatability of the proposed system was also investigated. The positioning tests were repeated ten times to ensure the reproducibility. The initial and target positions in each test remain the same as abovementioned. The measured target position and the calculated positioning accuracy (3σ) are concluded in Table III. The root-mean-square (RMS) of $T_x/T_y/T_z/R_x/R_y/R_z$ are 10.0003 μm , 10.0023 μm , 9.9961 μm , 100.0042 μrad , 99.9593 μrad , and 99.9715 μrad , respectively, which can be obtained as

$$X_{\text{RMS}} = \sqrt{\frac{1}{N} \sum_{i=1}^N X_i^2} = \sqrt{\frac{X_1^2 + X_2^2 + \dots + X_N^2}{N}} \quad (14)$$

where N is the number of samples and X is the variable.

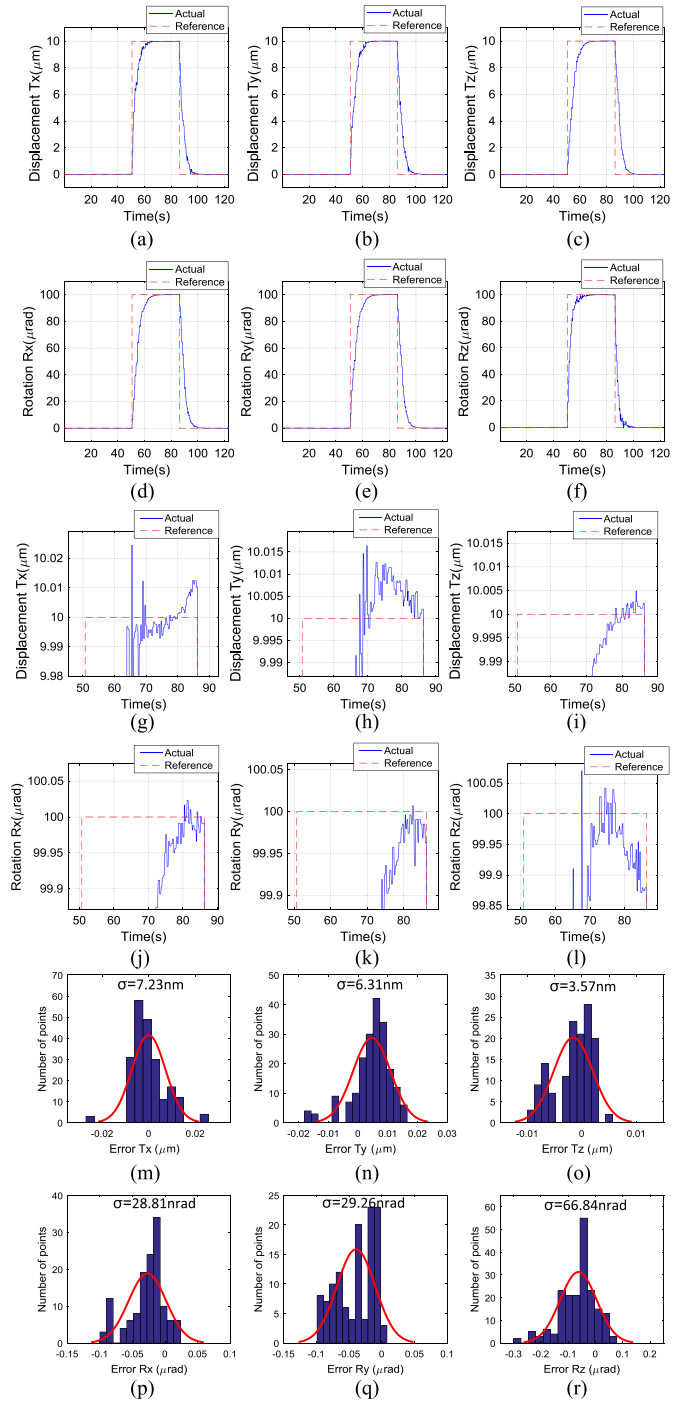


Fig. 9. Positioning results in the six axes. (a)–(f) Time history of positioning. (g)–(l) Steady-state error magnification diagram. (m)–(r) Histograms of steady-state errors of the positioning system.

The standard deviations (σ) of $T_x/T_y/T_z/R_x/R_y/R_z$ are 0.0099, 0.0047, 0.0022, 0.0194, 0.0282, and 0.0632, respectively, which can be obtained as follows:

$$\sigma = \sqrt{\frac{1}{N-1} \sum_{i=1}^N (X_i - \mu)^2} \quad (15)$$

where μ is the sample mean.

TABLE III
POSITIONING REPEATABILITY OF THE 6-DOF SYSTEM

N o.	Perf.	Tx	Ty	Tz	Rx	Ry	Rz
1	Mean	10.012	9.995	9.998	100.00 8	99.982	99.893
	σ	7.931	6.474	2.279	18.567	13.620	23.503
	3σ	23.793	19.422	6.836	55.700	40.861	70.508
2	Mean	10.015	10.002	9.996	100.01 8	99.894	99.924
	σ	8.778	5.471	2.069	20.184	28.138	80.375
	3σ	26.335	16.412	6.206	60.553	84.414	241.12 6
3	Mean	10.009	10.004	9.997	100.01 3	99.983	99.883
	σ	8.954	7.914	2.160	24.066	24.848	96.748
	3σ	26.863	23.741	6.479	72.199	74.544	290.24 4
4	Mean	9.992	9.997	9.994	99.991	99.975	100.05 5
	σ	5.046	4.625	1.559	26.392	18.148	70.870
	3σ	15.139	13.874	4.676	79.176	54.444	212.61 0
5	Mean	10.006	10.005	9.992	100.03 5	99.928	100.02 0
	σ	6.501	5.820	1.180	32.008	16.412	35.182
	3σ	19.504	17.459	3.540	96.024	49.237	105.54 6
6	Mean	9.994	10.004	9.997	99.960	99.959	99.998
	σ	7.432	4.734	2.227	19.967	22.128	89.575
	3σ	22.296	14.201	6.800	59.900	66.385	268.72 4
7	Mean	9.992	10.005	9.996	100.00 1	99.965	100.01 1
	σ	6.332	8.179	2.270	29.948	22.839	98.656
	3σ	18.995	24.536	6.810	89.845	68.519	295.96 8
8	Mean	10.003	10.008	10.000	100.00 6	99.966	99.910
	σ	4.600	7.199	2.874	36.738	22.247	85.236
	3σ	13.799	21.597	8.622	110.21 4	66.740	255.70 9
9	Mean	9.994	10.007	9.996	100.00 4	99.959	100.03 6
	σ	5.622	5.131	2.185	32.870	19.511	93.574
	3σ	16.865	15.392	6.556	98.610	58.533	280.72 2
10	Mean	9.986	9.996	9.995	100.00 6	99.982	99.985
	σ	5.494	5.213	1.959	29.923	32.127	77.528
	3σ	16.481	15.638	5.876	89.771	96.380	232.58 4

Units:
Mean $T_x/T_y/T_z$ (μm), $R_x/R_y/R_z$ (μrad).
 σ $T_x/T_y/T_z$ (nm), $R_x/R_y/R_z$ (nrad).
 3σ $T_x/T_y/T_z$ (nm), $R_x/R_y/R_z$ (nrad).

The positioning repeatability in 3σ of the proposed positioning system is better than $30\text{ nm} \times 30\text{ nm} \times 15\text{ nm} \times 150\text{ nrad} \times 150\text{ nrad} \times 300\text{ nrad}$ in the 3-D space.

B. Discussions on System Performance

In order to make a comparison with some already reported 6-DOF systems, several typical performances of the present proposed system are given in Table IV.

With an open-loop controlling, a large stroke of $\pm 0.04\text{ mm} \times \pm 0.04\text{ mm} \times \pm 0.03\text{ mm} \times \pm 0.2\text{ mrad} \times \pm 0.2\text{ mrad} \times \pm 0.3\text{ mrad}$ can be achieved with the present proposed system. It should be noted that the stroke of this presented system is conservative due to the installation errors and the limited working displacement of the driving motor. If a larger travel

TABLE IV
PERFORMANCE COMPARISONS FOR THE PROPOSED SYSTEM

Ref.	Diameter \times height	Resolution	Workspace	Accuracy(3σ)
[22]	unknown	unknown	$0.0082 \times 0.0105 \times 0.013 \times 0.224 \times 0.105 \times 0.097$	unknown
[23]	unknown	$0.1 \times 0.1 \times 0.1 \times 1 \times 1 \times 1$	$\pm 0.05 \times \pm 0.05 \times \pm 0.15 \times \pm 0.733 \times \pm 0.733 \times \pm 0.244$	unknown
[24]	173.2×50	$0.005 \times 0.005 \times 0.005 \times 0.7 \times 0.7 \times 0.7$	$0.008 \times 0.008 \times 0.008 \times 0.2 \times 0.2 \times 0.2$	unknown
[25]	350×120	$0.015 \times 0.015 \times 0.015 \times 0.678 \times 0.678 \times 0.678$	$2 \times 2 \times 2 \times 34.907 \times 34.907 \times 34.907$	unknown
[27]	250×80	$0.004 \times 0.004 \times 0.004 \times \text{unknown} \times \text{unknown} \times \text{unknown}$	$\pm 0.04 \times \pm 0.04 \times \pm 0.08 \times \pm 0.8 \times \pm 0.8 \times \pm 0.4$	$0.033 \times 0.033 \times 0.084 \times 0.21 \times 0.9 \times 0.9$
This work	264×148.4	$0.01 \times 0.01 \times 0.005 \times 0.1 \times 0.1 \times 0.2$	$\pm 0.04 \times \pm 0.04 \times \pm 0.03 \times \pm 0.2 \times \pm 0.2 \times \pm 0.3$	$0.03 \times 0.03 \times 0.015 \times 0.15 \times 0.15 \times 0.3$

Units:
Diameter \times height (mm \times mm).
Resolution $T_x/T_y/T_z$ (μm), $R_x/R_y/R_z$ (μrad).
Workspace $T_x/T_y/T_z$ (mm), $R_x/R_y/R_z$ (mrad).
Accuracy(3σ) $T_x/T_y/T_z$ (μm), $R_x/R_y/R_z$ (μrad).

range is demanded, the stroke of the proposed system may be further increased by using a linear motor with a larger working displacement, such as voice coil motors.

Moreover, the properties of utilized sensors have significant influences on the positioning tests. The capacitive displacement sensor, which is a noncontact device capable of high-resolution measurement of the position, is adopted in this research. It is advantageous to precision positioning. Capacitive displacement sensors can be used to measure the position of the objects down to the nanometer level. Even though the capacitive displacement sensors with a compact design are utilized, the signal noise from the sensor cannot be ignored in the nanometer level positioning process. Hence, an advanced signal processing technique should be developed in the following step to efficiently filter out noises. A high-precision grating with low-noise generation may be used for further improving the position resolution of the proposed positioning system. It is hoped that the positioning accuracy may be increased from tens of nanometers to several nanometers with the proposed system.

Additionally, the 3σ positioning accuracy of the proposed system can be achieved about 30 nm in linear position control and $0.3\text{ }\mu\text{rad}$ in angular position control, which is advanced in the present proposed 6-DOF positioning systems. Comparing the closed-loop positioning with the open-loop positioning, the standard deviations of $T_x/T_y/T_z/R_x/R_y/R_z$ are reduced from $0.0326\text{ }\mu\text{m}/0.0383\text{ }\mu\text{m}/0.0201\text{ }\mu\text{m}/0.41315\text{ }\mu\text{rad}/0.4598\text{ }\mu\text{rad}/0.9404\text{ }\mu\text{rad}$ to $0.0099\text{ }\mu\text{m}/0.0047\text{ }\mu\text{m}/0.0022\text{ }\mu\text{m}/0.0194\text{ }\mu\text{rad}/0.0282\text{ }\mu\text{rad}/0.0632\text{ }\mu\text{rad}$. The positioning accuracy is obviously improved.

In ultraprecision optical engineering, the posture of some optical elements needs to be adjusted in 6-DOF with several tens of nanometers position resolution and within several tens of micrometers workspace. For example, the alignment of optical elements in lithographic projection lenses [3], [34].

Although commercial 6-DOF positioning systems have enough workspace, the position resolution and positioning accuracy can not satisfy the requirements. Furthermore, the mechanism proposed in this article is made of stainless steel 431. The thermal expansion coefficient of this material is close to that in optical glasses. The 6-DOF positioning system proposed in this article has a practical prospect in the above-mentioned ultraprecision optical engineering. The proposed system is more advantaged than the present commercial ones in achieving the high-precision positioning accuracy. In order to improve the position tracking accuracy and the response speed of the system, a more compact 6-DOF positioning system will be developed by optimizing the structural design in the future research works. Some advanced control strategies, i.e., discrete-time repetitive control [8], enhanced model-predictive control [14], sliding-mode control [35], and fuzzy adaptive control [36], will be adopted.

VII. CONCLUSION

This article proposed a parallel 6-DOF positioning system with high resolution, high repeatability, and low parasitic motion. Lever-bipod-lever was adopted to design the limb with input displacement reduction, which improves the position resolution of the end effector. Based on the matrix method, a compliance model of the proposed mechanism was built. The output compliance, input stiffness, and stroke of the proposed mechanism were theoretically calculated. As following, the feasibility of the proposed numerical model was also verified by an FEA simulation process. Furthermore, a prototype was manufactured for experimental investigations. The travel range of the proposed system can achieve $\pm 40 \mu\text{m} \times \pm 40 \mu\text{m} \times \pm 30 \mu\text{m} \times \pm 200 \mu\text{rad} \times \pm 200 \mu\text{rad} \times \pm 300 \mu\text{rad}$ with the resolution of $10 \text{ nm} \times 10 \text{ nm} \times 5 \text{ nm} \times 100 \text{ nrad} \times 100 \text{ nrad} \times 200 \text{ nrad}$ in an open-loop control. The positioning accuracy of the six axes can achieve $30 \text{ nm} \times 30 \text{ nm} \times 15 \text{ nm} \times 150 \text{ nrad} \times 150 \text{ nrad} \times 300 \text{ nrad}$ in closed-loop control. The experimental results not only validate the effectiveness of the proposed positioning system but also verify the nanometer-scale spatial positioning accuracy within several tens of micrometers stroke range. The proposed micro/nanopositioning system may expand the actual application of alignment optical elements in projection lenses of 193 nm immersion lithography.

In the future, some research works can be carried out to improve the applicability of the proposed 6-DOF positioning system: High-performance control strategies will be carried and high-speed tracking performance will be investigated, and the geometrical dimension of the proposed mechanism will be optimized and miniaturized.

REFERENCES

- [1] Y. K. Yong, B. Bhikkaji, and S. O. R. Moheimani, "Design, modeling, and FPAA-based control of a high-speed atomic force microscope nanopositioner," *IEEE/ASME Trans. Mechatron.*, vol. 18, no. 3, pp. 1060–1071, Jun. 2013.
- [2] M. Maroufi and S. O. R. Moheimani, "An SOI-MEMS piezoelectric torsional stage with bulk piezoresistive sensors," *IEEE Sensors J.*, vol. 17, no. 10, pp. 3030–3040, May 2017.
- [3] T. J. Teo, G. Yang, and I.-M. Chen, "A large deflection and high payload flexure-based parallel manipulator for UV nanoimprint lithography: Part I. Modeling and analyses," *Precis. Eng.*, vol. 38, pp. 861–871, 2014.
- [4] Z. Zhu, S. To, K. F. Ehmann, and X. Zhou, "Design, analysis, and realization of a novel piezoelectrically actuated rotary vibration system for micro-/nanomachining," *IEEE/ASME Trans. Mechatron.*, vol. 22, no. 3, pp. 1227–1237, Jun. 2017.
- [5] S. T. Smith, *Flexures: Elements of Elastic Mechanisms*. Boca Raton, FL, USA: CRC Press, 2000.
- [6] L. L. Howell, *Compliant Mechanisms*. New York, NY, USA: Wiley, 2001.
- [7] D. Hwang, J. Byun, J. Jeong, and M. G. Lee, "Robust design and performance verification of an in-plane XY θ micropositioning stage," *IEEE Trans. Nanotechnol.*, vol. 10, no. 6, pp. 1412–1423, Nov. 2011.
- [8] B. J. Kenton and K. K. Leang, "Design and control of a three-axis serial-kinematic high-bandwidth nanopositioner," *IEEE/ASME Trans. Mechatron.*, vol. 17, no. 2, pp. 356–369, Apr. 2012.
- [9] S. P. Wadikhaye, Y. K. Yong, and S. O. R. Moheimani, "A serial-kinematic nanopositioner for high-speed atomic force microscopy," *Rev. Sci. Instrum.*, vol. 85, 2014, Art. no. 105104.
- [10] Y. Qin, B. Shirinzadeh, Y. Tian, D. Zhang, and U. Bhagat, "Design and computational optimization of a decoupled 2-DOF monolithic mechanism," *IEEE/ASME Trans. Mechatron.*, vol. 19, no. 3, pp. 872–881, Jun. 2014.
- [11] Y. Li and Q. Xu, "Development and assessment of a novel decoupled XY parallel micropositioning platform," *IEEE/ASME Trans. Mechatron.*, vol. 15, no. 1, pp. 125–135, Feb. 2010.
- [12] S. Polit and J. Dong, "Development of a high-bandwidth XY nanopositioning stage for high-rate micro-/nanomanufacturing," *IEEE/ASME Trans. Mechatron.*, vol. 16, no. 4, pp. 724–733, Aug. 2011.
- [13] L. Clark, B. Shirinzadeh, Y. Tian, and B. Yao, "Development of a passive compliant mechanism for measurement of micro/nanoscale planar 3-DOF motions," *IEEE/ASME Trans. Mechatron.*, vol. 21, no. 3, pp. 1222–1232, Jun. 2016.
- [14] Q. Xu, "New flexure parallel-kinematic micropositioning system with large workspace," *IEEE Trans. Robot.*, vol. 28, no. 2, pp. 478–491, Apr. 2012.
- [15] Y. K. Yong, S. O. R. Moheimani, B. J. Kenton, and K. K. Leang, "Invited review article: High-speed flexure-guided nanopositioning: Mechanical design and control issues," *Rev. Sci. Instrum.*, vol. 83, 2012, Art. no. 121101.
- [16] Y. Jiang, T. Li, and L. Wang, "Design, development, and application of a compact flexure-based decoupler with high motion transmission efficiency and excellent input decoupling performance," *IEEE/ASME Trans. Mechatron.*, vol. 22, no. 2, pp. 1071–1081, Apr. 2017.
- [17] S. Awatar and A. H. Slocum, "Design of parallel kinematic XY flexure mechanisms," in *Proc. ASME Int. Des. Eng. Tech. Conf. Comput. Inf. Eng. Conf.*, Long Beach, CA, USA, 2005, pp. 89–99.
- [18] Z. Du, R. Shi, and W. Dong, "A piezo-actuated high-precision flexible parallel pointing mechanism: Conceptual design, development, and experiments," *IEEE Trans. Robot.*, vol. 30, no. 1, pp. 131–137, Feb. 2014.
- [19] Y. Li and Q. Xu, "Design and analysis of a totally decoupled flexure-based XY parallel micromanipulator," *IEEE Trans. Robot.*, vol. 25, no. 3, pp. 645–657, Jun. 2009.
- [20] Z. Guo, Y. Tian, X. Liu, B. Shirinzadeh, F. Wang, and D. Zhang, "An inverse Prandtl-Ishlinskii model based decoupling control methodology for a 3-DOF flexure-based mechanism," *Sensors Actuators A, Phys.*, vol. 230, pp. 52–62, 2015.
- [21] J.-J. Kim, Y.-M. Choi, D. Ahn, B. Hwang, D.-G. Gweon, and J. Jeong, "A millimeter-range flexure-based nano-positioning stage using a self-guided displacement amplification mechanism," *Mechanism Mach. Theory*, vol. 50, pp. 109–120, 2012.
- [22] K. Cai, Y. Tian, F. Wang, D. Zhang, X. Liu, and B. Shirinzadeh, "Design and control of a 6-degree-of-freedom precision positioning system," *Robot. Comput.-Integr. Manuf.*, vol. 44, pp. 77–96, 2017.
- [23] H. Shin and J.-H. Moon, "Design of a double triangular parallel mechanism for precision positioning and large force generation," *IEEE/ASME Trans. Mechatron.*, vol. 19, no. 3, pp. 862–871, Jun. 2014.
- [24] T.-L. Wu, J.-H. Chen, and S.-H. Chang, "A six-DOF prismatic-spherical parallel compliant nanopositioner," *IEEE Trans. Ultrason., Ferroelect., Freq. Control*, vol. 55, no. 12, pp. 2544–2551, Dec. 2008.
- [25] D. Kang and D. Gweon, "Development of flexure based 6-degrees of freedom parallel nano-positioning system with large displacement," *Rev. Sci. Instrum.*, vol. 83, 2012, Art. no. 035003.
- [26] K. M. Varadarajan and M. L. Culpepper, "A dual-purpose positioner-fixture for precision six-axis positioning and precision fixturing: Part I. Modeling and design," *Precis. Eng.*, vol. 31, pp. 276–286, 2007.

- [27] K. M. Varadarajan and M. L. Culpepper, "A dual-purpose positioner-fixture for precision six-axis positioning and precision fixturing: Part II. Characterization and calibration," *Precis. Eng.*, vol. 31, pp. 287–292, 2007.
- [28] Y. Yue, F. Gao, X. Zhao, and Q. J. Ge, "Relationship among input-force, payload, stiffness, and displacement of a 6-DOF perpendicular parallel micromanipulator," *J. Mechanisms Robot.*, vol. 2, Feb. 2010, Art. no. 011007.
- [29] F. Gao, W. Li, X. Zhao, Z. Jin, and H. Zhao, "New kinematic structures for 2-, 3-, 4-, and 5-DOF parallel manipulator designs," *Mechanism Mach. Theory*, vol. 37, pp. 1395–1411, 2002.
- [30] L. C. Hale, "Principles and techniques for designing precision machines," Ph.D. dissertation, Dept. Mech. Eng., Massachusetts Inst. Technol., Cambridge, MA, USA, 1999.
- [31] Y.-Q. Yu, L. L. Howell, C. Lusk, Y. Yue, and M.-G. He, "Dynamic modeling of compliant mechanisms based on the pseudo-rigid-body model," *J. Mech. Des.*, vol. 127, no. 4, pp. 760–765, 2005.
- [32] Y. Tian, B. Shirinzadeh, D. Zhang, and Y. Zhong, "Three flexure hinges for compliant mechanism designs based on dimensionless graph analysis," *Precis. Eng.*, vol. 34, pp. 92–100, 2010.
- [33] N. Lobontiu, *Compliant Mechanisms: Design of Flexure Hinges*. Boca Raton, FL, USA: CRC Press, 2002.
- [34] K. Guo, M. Ni, H. Chen, and Y. Sui, "A monolithic adjusting mechanism for optical element based on modified 6-PSS parallel mechanism," *Sensors Actuators A, Phys.*, vol. 251, pp. 1–9, 2016.
- [35] S. Xiao and Y. Li, "Optimal design, fabrication, and control of an XY micropositioning stage driven by electromagnetic actuators," *IEEE Trans. Ind. Electron.*, vol. 60, no. 10, pp. 4613–4626, Oct. 2013.
- [36] P. Li, P. Li, and Y. Sui, "Adaptive fuzzy hysteresis internal model tracking control of piezoelectric actuators with nanoscale application," *IEEE Trans. Fuzzy Syst.*, vol. 24, no. 5, pp. 1246–1254, Oct. 2016.



Defu Zhang received the B.S. and Ph.D. degrees in mechanical engineering from Harbin Engineering University, Harbin, China, in 2007 and 2012, respectively.

From 2012 to 2018, he was an Assistant Researcher with the State Key Laboratory of Applied Optics, Changchun Institute of Optics, Fine Mechanics and Physics (CIOMP), Chinese Academy of Science, Changchun, China. Since 2018, he has been an Assistant Researcher with the Department of Advanced Space Technology,

CIOMP, Chinese Academy of Science. His research interests include micro/nanopositioning systems, ultraprecise mechatronics, and optomechanical systems design.



Pengzhi Li received the B.S. degree in mechanical engineering from the Harbin Institute of Technology, Harbin, China, in 2006, and the M.S. degree in mechatronics engineering from Shanghai Jiao Tong University, Shanghai, China, in 2011. He is currently working toward the Ph.D. degree in mechatronics engineering with the University of the Chinese Academy of Sciences, Beijing, China.

From 2011 to 2013, he was a Research Assistant with the State Key Laboratory of Applied

Optics (SKLAO), Changchun Institute of Optics, Fine Mechanics and Physics (CIOMP), Chinese Academy of Science, Changchun, China. From 2013 to 2018, he was an Assistant Researcher with the SKLAO, CIOMP, Chinese Academy of Science. His research interests include ultraprecise mechatronics and control of piezoelectric actuators modeling.



Jianguo Zhang received the B.S. and M.S. degrees in mechanical engineering from the Harbin Institute of Technology, Harbin, China, in 2008 and 2010, respectively, and the Ph.D. degree from the Department of Mechanical Science and Engineering, Nagoya University, Nagoya, Japan, in 2014.

From 2014 to 2017, he was an Assistant Researcher with the State Key Laboratory of Applied Optics, Changchun Institute of Optics, Fine Mechanics and Physics, Chinese Academy of Science, Changchun, China. From 2017 to 2018, he was a designated Assistant Professor with Department of Aerospace Engineering, Nagoya University, Nagoya, Japan. His research interests include elliptical vibration cutting technology and the precise fabrication of functional micro/nano structures on difficult-to-cut materials.

Dr. Zhang is a recipient of the Young Researcher Award in Japan Society for Precision Engineering 2015.



Huanan Chen received the B.S. degree in mechanical engineering from Harbin Engineering University, Harbin, China, in 2007, and the M.S. degree in mechanical engineering from the Harbin Institute of Technology, Harbin, China, in 2011.

From 2011 to 2013, he was a Research Assistant with the State Key Laboratory of Applied Optics (SKLAO), Changchun Institute of Optics, Fine Mechanics and Physics (CIOMP), Chinese Academy of Science, Changchun, China. From

2013 to 2018, he was an Assistant Researcher with the SKLAO, CIOMP, Chinese Academy of Science. His research interests include ultraprecise mechanism design and optimization.



Kang Guo received the B.S. and Ph.D. degrees in mechanical engineering from Jilin University, Changchun, China, in 2006 and 2011, respectively.

From 2012 to 2014, he was an Assistant Researcher with the State Key Laboratory of Applied Optics (SKLAO), Changchun Institute of Optics, Fine Mechanics and Physics (CIOMP), Chinese Academy of Science, Changchun, China. From 2014 to 2018, he was an Associate Research Fellow with the SKLAO, CIOMP, Chi-

nese Academy of Science. His research interests include ultraprecise actuation and measurement for optomechanical systems.



Mingyang Ni received the B.S. and M.S. degrees in mechatronics engineering from Jilin University, Changchun, China, in 2006 and 2009, respectively.

From 2009 to 2016, he was an Assistant Researcher with the State Key Laboratory of Applied Optics (SKLAO), Changchun Institute of Optics, Fine Mechanics and Physics (CIOMP), Chinese Academy of Science, Changchun, China. From 2016 to 2018, he was an Associate Research Fellow with the SKLAO, CIOMP, Chi-

nese Academy of Science. His research interests include ultraprecise mechanism design and assembling.